HIGH ENERGY COMPONENT OF X-RAY SPECTRA IN ECR ION SOURCES

J.Y. Benitez[1*], J.D. Noland[1], D. Leitner[1], C. Lyneis[1], D.S. Todd[1], and J. Verboncoeur[2]
[1]One Cyclotron Road, LBNL, Berkeley, CA 94720, U.S.A.

[2]Department of Nuclear Engineering, UCB, 4155 Etcheverry Hall, Berkeley, CA 94720, U.S.A.

[*] Corresponding author: jybenitez@lbl.gov

Abstract

The 88-Inch Cyclotron at LBNL is home to three powerful ECR ion sources, which operate at a range of heating frequencies from 6.4 GHz for the ECR to a combination of 18GHz and 28GHz for the VENUS superconducting ECR. Over the last few years we have investigated the production of x-rays from ECR ion sources with the goal of improving the understanding of the electron energy distribution within these sources. By measuring the spectral temperatures (defined as the reciprocal of the slope of the semi-logarithmic plot of the x-ray energy spectra) and using them as relative indicators of the electron temperatures, different plasma conditions and tuning parameters can be evaluated. A comparison of the axial x-ray spectra measured with the 6.4GHz ECR ion source to spectra obtained using the 18 and 28GHz VENUS source at equivalent power densities is presented. In addition, the paper discusses the experimental setup and analysis of the x-ray measurements. In particular, we discuss how to remove artifacts from the energy spectra resulting from the interaction of x-rays with the detector in order to accurately represent the x-rays emitted from the source.

INTRODUCTION

Lawrence Berkeley National Lab (LBNL) has three electron cyclotron resonance ion sources (ECRIS): LBNL-ECR, AECR-U, and VENUS, which operate at frequencies of 6.4GHz, 10 & 14GHz, and 18 & 28 GHz, respectively. This wide range of operating frequencies presents a unique opportunity to examine how various plasma parameters scale with frequency.

Several interactions lead to the emission of bremsstrahlung by electrons, in the form of x-rays. For example, electrons colliding with ions and electrons which are lost from the plasma and collide with the plasma chamber wall radiate x-rays due to their sudden deceleration. Studying the radiated x-ray spectra is a step towards our ultimate goal of determining the electron energy distribution function (EEDF).

The difficulty preventing one from making direct conclusions of the EEDF from an x-ray spectrum is that the detected spectrum does not directly reflect the energy of the electrons in the plasma and the spectra emitted by such a distribution. The detected spectrum is a result of many parameters. For example, the detector, a thallium-activated sodium iodine (Na(Tl)) scintillator, reacts differently to photons depending on their energy and the dimensions of the scintillator itself. Correcting the detected spectra so that they more accurately represent the emitted spectra is crucial in our attempt to characterize the plasma electrons. In addition the bremsstrahlung coming from the walls must be separated from the bremsstrahlung coming from the electron-ion collisions inside the plasma, since we want to measure the EEDF of the confined plasma and not the EEDF of the electrons lost to the walls. Therefore, specific collimation of the emitted x-rays is necessary in order to minimize the amount of wall bremsstrahlung visible to the detector.

The data presented in this paper include bremsstrahlung measurements from the VENUS ion source when using 18GHz and 28GHz heating and bremsstrahlung measurements from the LBNL-ECR ion source using 6.4GHz heating, both emitted axially and observed through the extraction aperture. The emitted x-rays are collimated and then detected with a NaI(Tl) scintillator. The specific collimation, which controls the region visible to the detector, and its significance, is discussed as well as the response of the NaI(Tl) detector to the x-rays and the correction applied. Finally, a preliminary comparison is made between the LBNL-ECR and VENUS bremsstrahlung emitted at equivalent plasma power densities and similar collimation geometries.

EXPERIMENTAL SETUP

Collimation and Detector

The experimental setup and collimation geometry for both VENUS and LBNL-ECR spectra were designed to minimize background radiation from other sources such as the nearby AECR-U. Despite the effort to shield the detector from the AECR-U's x-rays, background measurements showed that the background was minimized but not completely eliminated. Figure 1 shows the significance of the background for LBNL-ECR spectra at low power, at which the x-ray intensity is relatively low in comparison. Note, in particular, for a spectrum taken at a low power of 115W, as shown, the counts are only a factor of ~2 greater than the background.

ECR

The experimental setup of the LBNL-ECR and NaI detector is shown in Figure 2. The collimation consists of

two copper blocks and one Heavymet (95% W and 5% Cu) block. Copper was chosen despite lower density than lead because the 0.100 m copper block effectively absorbs x-rays below 1 MeV.

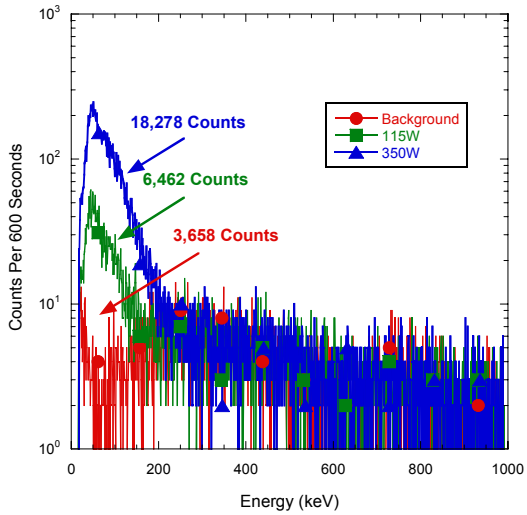

Figure 1. The background x-ray spectrum is high compared to the ECR spectra at low power.

Furthermore copper does not have absorption edges in the range of energies we are interested in. This decreases the probability of characteristic x-rays, produced by photoelectric absorption in the copper, from entering the detector. The first collimator, a copper block, is located inside of the bending magnet vacuum chamber, 2.75m after the extraction aperture. It is 100mm long and has a 10mm square aperture. The purpose of this first collimator is to lower the number of x-rays that can enter the remaining three collimators at large angles with respect to the collimation axis, and thus reduce the number of scattered x-rays that reach the detector. The second collimator, Heavymet (95% W and 5% Cu), located 35mm behind the first collimator, is 127mm long and has a 1mm square aperture. The third collimator, copper, located 2.7 m after the second collimator, is 100 mm long and has a 3 mm square aperture. A fourth collimator, 51mm long with a 13mm circular aperture and made of lead, is located directly before the detector. The geometric acceptance angle of this collimator system is approximately 0.04 deg. This corresponds to a 5mm square area at the 8mm diameter extraction aperture. By ensuring that the detector does not see any solid walls at the extraction end of the plasma chamber, we minimize the chances of detecting wall bremsstrahlung, or x-rays produced by thick-target interactions.

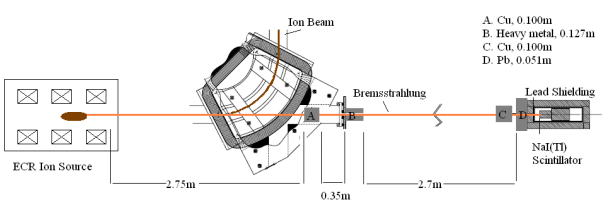

Figure 2. ECR x-ray collimation and detection setup.

VENUS

The experimental setup of the VENUS ion source and NaI detector is shown in Figure 3. The first collimator, 2.37m after the extraction aperture, is a 127mm long Heavymet collimator with a 1mm square aperture. The NaI(Tl) and photomultiplier (PMT) detector system follows the first collimator by 2.16m. In addition a second collimator is placed directly before the detector. The second collimator, made of lead, is 51mm long with a 13mm diameter aperture. The experimental setup results in a 14mm square area visible to the detector at the extraction aperture. Since VENUS' extraction aperture is only 8mm in diameter, all of the VENUS spectra shown in this paper contain wall bremsstrahlung.

In order to compare VENUS spectra with the LBNL-ECR spectra, the second copper collimator is removed from the LBNL-ECR setup. With this removal, the LBNL-ECR and VENUS detection setups both see a 14 mm square area at their 8 mm diameter extraction apertures. Differences in x-ray spectra for the two LBNL-ECR collimator setups are discussed in the next section.

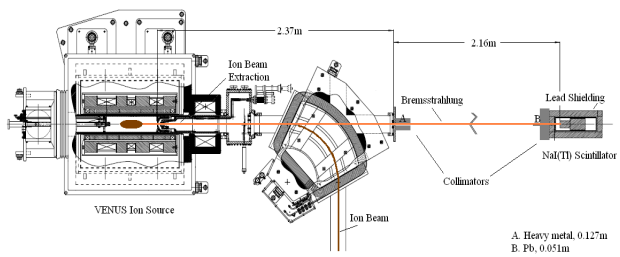

Figure 3. VENUS x-ray collimation and detection setup.

Influence of Wall Bremsstrahlung on X-Ray Spectra

A study was undertaken to compare x-ray spectra for which the area visible to the detector includes the extraction wall of the plasma chamber to ones for which only the bulk plasma is visible. First we note that the extraction aperture of the LBNL-ECR has a diameter of 8 mm. As discussed in the previous section, two collimation setups were used for LBNL-ECR spectra. One setup, with collimator "C" in Figure 2 removed, allows the detector to see a 14 mm square area at the extraction aperture, ensuring that extraction-end wall is visible to the detector. The second setup provides a 5mm square area visible to the detector, ensuring that no extraction-end wall is visible. In Figure 4 one compares the two setups and it can be seen that the number of recorded counts and the shape of the spectra change when the extraction plate is visible.

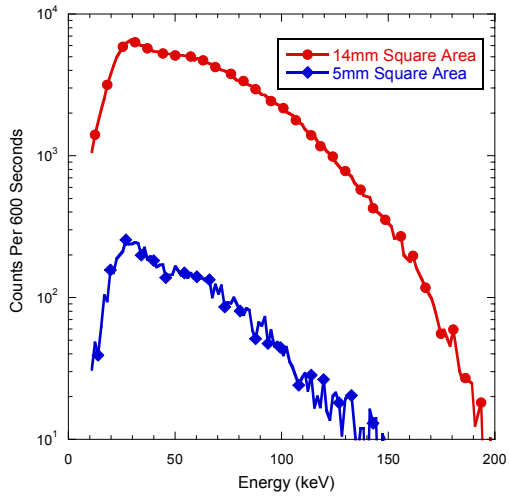

Figure 4. LBNL-ECR X-ray spectra at 300W of 6.4GHz power recorded with a 5mm square area versus a 14mm square area visible to the detector at the 8mm circ3ular diameter extraction aperture.

A possible explanation for these results is that unconfined electrons stream towards and hit the extraction plate emitting thick-target bremsstrahlung. The presence of thick-target bremsstrahlung overwhelms bremsstrahlung produced in the plasma [1]. As shown in [1], the electron bremsstrahlung emissivity can be written as:

$$J(h\upsilon) = \int_{h\upsilon}^{\infty} j(E,h\upsilon) v g(E) dE \qquad (1)$$

where v is the electron velocity, g(E) is the EEDF, E is the electron energy, hυ is the energy radiated, and where $j(E,h\upsilon)$, the energy radiated per electron, is given by

$$j_{at}(E,h\upsilon) = 1.43\times10^{-28} N_{at} \frac{Z^2}{E} \Delta z \qquad (2)$$

for thin-target bremsstrahlung, and by

$$j_{sol}(E,h\upsilon) = 1.10\times10^{-5} \frac{Z_{sol}}{l} (E - h\upsilon) \qquad (3)$$

for thick-target bremsstrahlung, where N_{at} is atomic density, Z_{sol} is the atomic number, E is the electron energy, and l is a constant on the order of one. Equation (1) is applicable to plasma bremsstrahlung as well. One detail to notice about the equations for $j_{at}(E,h\upsilon)$ and $j_{sol}(E,h\upsilon)$ is the size of the constant coefficient. Because the size of the coefficient is so much larger for thick-target bremsstrahlung its contribution to the recorded x-ray spectra is significant, as is apparent in Figure 4. For this reason, proper collimation is important.

NaI(Tl) Detector Efficiency

For our measurements, a 3-in. diameter by 3-in. long NaI(Tl) scintillator was utilized. To correct the x-ray spectra for detection efficiency, the detector was characterized in terms of scintillator material, scintillator size, and photon energy.

The scintillator produces pulses of light that are converted to an electric pulse by a photomultiplier tube (PMT) which is recorded by a multichannel analyzer (MCA). However, the recorded spectrum does not directly reflect the photon spectrum emitted by the electrons that reaches the detector. Several processes that can change the recorded spectrum take place before the photons are recorded in the data acquisition system.

First, the photons emitted by the electrons undergo attenuation and scattering in the media they traverse before reaching the detector. The media the photons pass through are a 3mm thick vacuum quartz window and approximately 2.7m of air (LBNL-ECR data) or 2.2m of air (VENUS data), and a thin layer, ~0.5mm, of aluminum that surrounds the NaI(Tl) scintillator. In addition, there is a finite probability that the photons will be detected at all by the 3-in.thick NaI(Tl) scintillator. The detection probability is slightly reduced for higher x-ray energies. The absorption efficiency of photons in these media is shown in Figure 5. The spectra in this paper are not corrected for this absorption resulting from media present between emission and detection. Nonetheless, it is important to note the poor representation of the low energy x-rays in the spectra. Future work will concentrate on detecting the low energy x-rays.

The second process the photons undergo has to do with the probability the detector will fully absorb them once they reach the detector and are detected. This probability arises from the interaction of the photons with the detector. A photon may be completely absorbed, resulting from photoelectric absorption. Also, a photon may be partially absorbed through Compton scattering with an absorbing recoil electron.

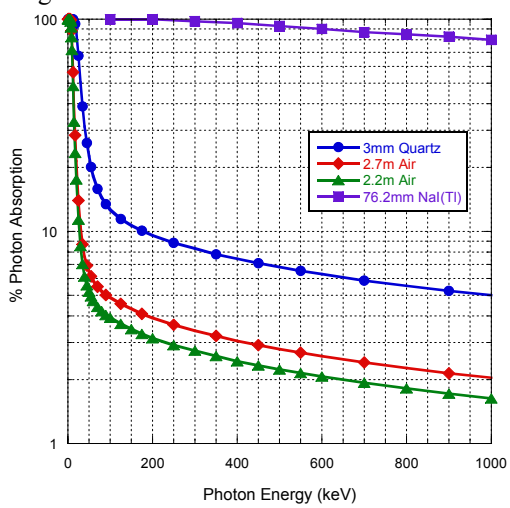

Figure 5. The absorption of photons in media decreases with increasing energy. See [2] for quartz and air attenuation coefficients. See [3] for a NaI(Tl) absorption curve.

The maximum energy that can be absorbed due to Compton scattering is called the Compton Edge, which

results from a 180° scattering angle between the photon and recoil electron, and is given by:

$$E_C = \frac{2E_\gamma^{\,2}}{m_e c^2 + 2E_\gamma} \quad (4)$$

where m_e is the electron mass and E_γ is the photon energy. Scattering at angles less then 180° gives rise to a Compton Plateau extending from zero to the Compton Edge. Backscatter peaks and pair production are not accounted for.

In other words, a photon emitted with energy K' has a certain probability of being fully detected, as energy K=K', or partially detected as an energy less than K', K<K'. The probability that a photon of energy K' is detected with energy K is given by the response matrix R(K',K) (See Figure 7).

In order to obtain the response matrix, R(K',K), one first needs the 3-in. x 3-in. NaI(Tl) scintillator's peak-to-total (P/T) curve from [6], shown in Figure 6, which gives the diagonal of the response matrix, shown in Table 1. The P/T curve describes the probability a photon's energy, K', when detected, is completely absorbed. Specifically, for a monoenergetic source of photons of energy K', the P/T is the ratio of counts detected in the full-energy peak, at K', to the total counts. Ideally, the monoenergetic source of photons would all be completely absorbed and a spectrum would show only a single line at energy K'. Data analysis was done using the published P/T 's from [6].

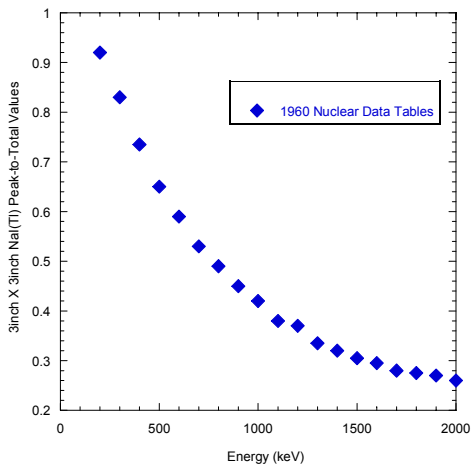

Figure 6. NaI(Tl) peak-to-total, P/T, curve from [6] compared with experimental findings. The values from [6] are approximate.

As previously stated, the P/T's are the diagonal of the response matrix R(K',K). In order to fill in the remainder of R(K',K), the P/T for each photon energy K' is subtracted from unity and the remainder is distributed equally amongst the Compton Plateau beginning with the Compton Edge, Equation 4, for the respective photon energy K'. As such, one approximation made is that the plateau is flat. A response matrix example is shown in Table 1 and Figure 7. For simplification, the response matrix used does not take into account the energy resolution of the detector in that the P/T is only assigned to one matrix element, corresponding to one energy value. This allows us to use a 100 element square response matrix.

K / K'	…	60 keV	100 keV	…	200 keV	300 keV	400 keV	…
100keV	…	0	**0.97**	…	0	0	0	…
200keV	…	0.012	0	…	**0.87**	0	0	…
300keV	…	0.013	0.013	…	0	**0.80**		…
400keV	…	0.014	0.014	…	0.014	0	**0.72**	…
⋮	⋮	⋮	⋮	⋮	⋮	⋮	⋮	⋮

Table 1. Response matrix elements. The matrix describes the probability a photon pf energy K' that reached the detector is detected as having an energy K. The diagonal, in bold, are the peak-to-total values for the scintillator.

As shown in [4], the relationship between the true photon spectrum I(K') and the detected spectrum P(K) is:

$$P(K) = \int_0^{K'_{max}} I(K') \cdot R(K', K) dK' \quad (5)$$

Discretely, the recorded spectra can be written as a series of linear equations:

$$P(K) = \sum_0^{K'_{max}} I(K') \cdot R(K', K) \quad (6)$$

This method of solving for the physical spectrum, free of detector influence, I(K'), is called direct matrix inversion [4,5]. The desired photon spectrum I(K') is obtained as follows:

$$I = PR^{-1} \quad (7)$$

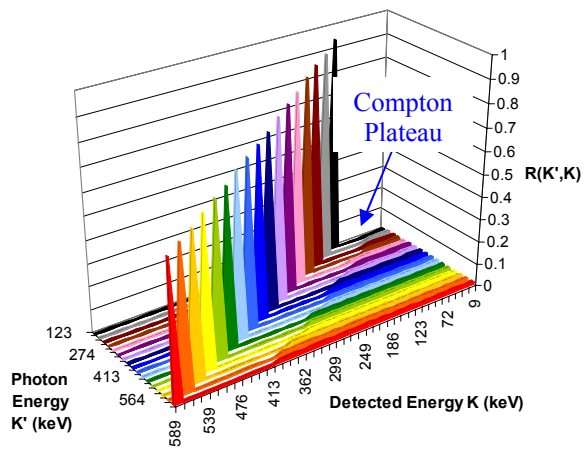

Figure 7. Example of a NaI(Tl) Response Matrix R(K',K) for photons of various energies.

Figure 8 shows an example of the results obtained when the direct matrix inversion method is applied. The amount of counts at the high energy end of the spectrum increase as counts are removed from the low energy end and placed into the high energy end.

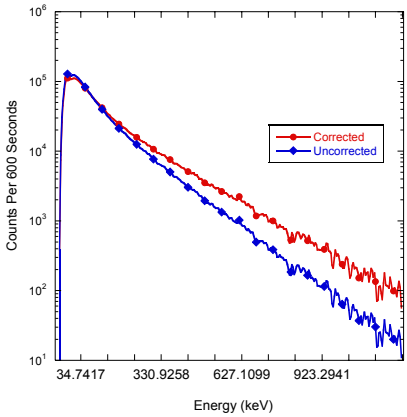

Figure 8. Applying the direct matrix inversion method corrects the detected spectra. The spectrum shown is from VENUS when operating at 1.5kW of 28GHz.

ANALYSIS

Our data analysis of the recorded spectra, using a code written in Python [7], is done in a number of steps. First, a background spectrum, such as shown in Figure 1, is subtracted from the x-ray spectra. The code then calibrates the x-ray spectra using a radioactive source spectrum that is recorded after each data set. The VENUS spectra, which often extend up to energies of 1MeV, are calibrated using a ^{207}Bi source with gamma-ray line energies of 569keV and 1063keV. The LBNL-ECR spectra, whose energies barely exceed 300keV, are calibrated using a ^{133}Ba source with a x-ray line energy of 31keV and gamma-ray line energies of 81keV, and 356keV. Once a spectrum has been calibrated it is corrected for detector efficiencies. Then its spectral temperature, T_S, is obtained using:

$$j(h\nu) \propto \exp\left(\frac{-h\nu}{kT_S}\right) \quad (8)$$

where hν is the energy of the radiated photon [8]. Using a semi-logarithmic representation of the data a least-squares fit is applied, from which the inverse of the slope is taken to represent the spectral temperature T_S. In addition to the T_S, the Python code also integrates the spectra for certain energy ranges to give the total amount of counts. The spectral temperatures and integrated count numbers are used as relative indicators of changes in the electron energy distribution as parameters such as power and frequency are varied.

RESULTS

X-Ray Spectra at Varying Powers

In Figure 9 VENUS x-ray spectra for a series of microwave powers at 28 GHz are shown.

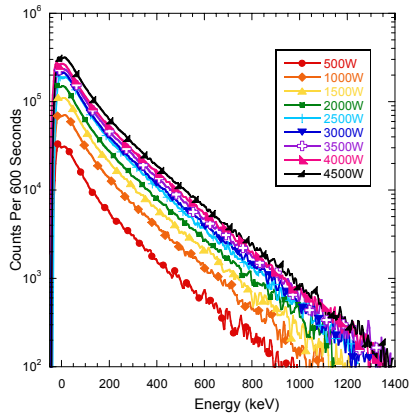

Figure 9. VENUS x-ray spectra for varying powers using 28GHz heating.

One trend that is immediately noticeable is that the slope remains relatively constant as microwave power is increased. Note, this can also be seen in Figure 10, which shows that the spectral temperature remains essentially constant with power. While we do not observe a strong increase in spectral temperature when increasing power, especially at higher microwave powers, there is a slight increase observable at very low powers.

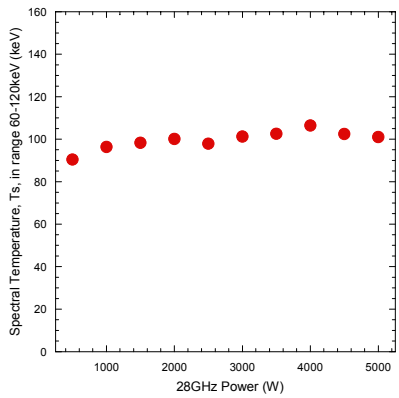

Figure 10. Spectral temperature for the 28GHz VENUS spectra, at various powers, in Figure 9.

The power radiated by the plasma per unit time in volume ΔV is [1]:

$$J_{pl}(h\nu) = (3.0\times10^{-21}) N_i N_e Z_i^2 \frac{1}{\sqrt{kT}} \exp\left(-\frac{h\nu}{kT}\right)\Delta V \quad (9)$$

where N_i is ion density, N_e is electron density, Z_i is ion atomic number, k is Boltzmann's constant, T is the electron temperature, and hυ is the energy of the radiated photon. From this equation it is obvious that the power radiated is linearly related to the electron density. A trend that can be deduced from Figure 11 is that the increase in x-ray counts is essentially linear with increased power. This result is consistent with results presented previously in references [9] and [10].

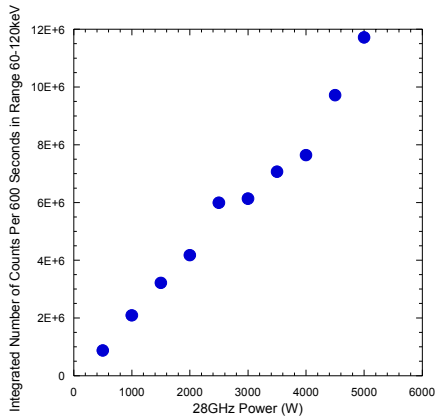

Figure 11. Integrated number of counts for 600 seconds over the energy range 60-120keV corresponding to the VENUS spectra in Figure 9.

Because the x-ray count is linearly dependent on density, and it is observed to increase linearly with power, it can be assumed that the primary effect of increasing power is to increase plasma density.

To show that increasing power does indeed cause density to rise, we can examine the behavior of the total particle current as power changes. To calculate the total particle current we use the recorded faraday cup (FC) current spectrum. The particle current is simply the FC current divided by the charge state of the particle. The total particle current, then, is the sum of particle currents for all species (Argon and Oxygen, in this case) and charge states present at a given power level. As shown in Figure 12, the particle current increases as power increases. This data corresponds to the data used to produce Figures 9-11, above. For similar confinement parameters, then, larger particle currents will principally be caused by larger plasma densities. Thus, plasma density increases with power.

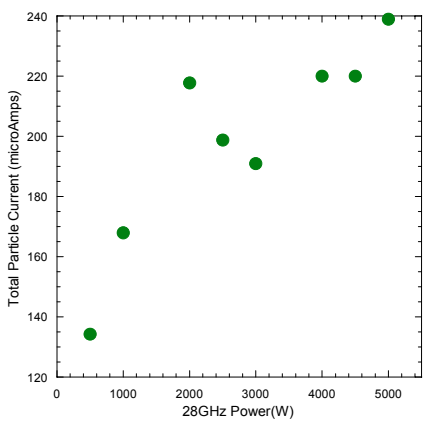

Figure 12. Total particle current corresponding to the VENUS spectra in Figure 9.

X-Ray Spectra at Varying Frequencies

Figure 13 shows calibrated x-ray spectra for 6.4GHz, 18GHz, and 28GHz at a roughly equivalent power density of ~2.3W/L. Note that for this comparison, using power per volume, the volume refers to the ECR zone and not the plasma chamber. We see an increase in the total recorded counts as well as the maximum recorded photon energy.

According to theory outlined in [11], increased microwave frequency causes both the electron density and mean energy of electrons to increase. Similarly, a larger mirror ratio, B_{max}/B_{min}, is predicted to lead to increases in both electron density and mean electron energy. For the data presented in Figure 13, the LBNL-ECR B_{max}/B_{min} ~2.3 while for VENUS B_{max}/B_{min} ~5. As such, when going from 6.4GHz (LBNL-ECR) to 18GHz (VENUS) the change in spectra is likely attributed to both increasing frequency and mirror ratio. On the other hand, for the VENUS data for 18GHz and 28GHz, the magnetic field ratios are identical and the only change is the frequency which causes the change in spectra shape.

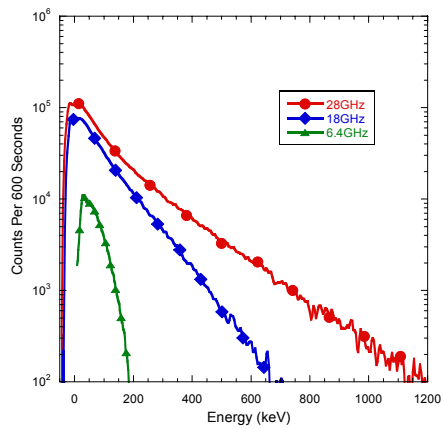

Figure 13. 6.4GHz (LBNL-ECR), 18GHz (VENUS), and 28GHz (VENUS) x-ray spectra at an equivalent power density of ~2.3kW/L.

Figure 14 shows a comparison of spectral temperatures for the three frequencies at equivalent power densities. There is an increase in spectral temperature when going from 6.4GHz to 18GHz of 40%. The increase from 18GHz to 28GHz is only 10%. The change in spectral temperature is a result of a change in the slope of the spectrum. The change in slope, or spectral temperature, indicates a change in the average electron energy in the plasma. Models [11] have shown that microwave heating frequency and the mirror ratio both change the mean energy of the electrons. Figure 14 reflects the change in mean energy as microwave heating frequency is changed.

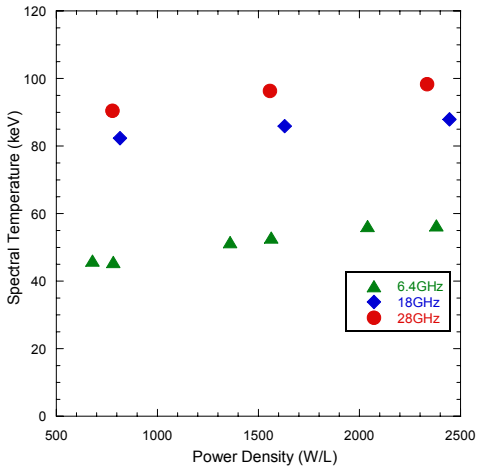

Figure 14. 6.4GHz (ECR, 50-100keV), 18GHz (VENUS, 60-120keV), and 28GHz (VENUS, 60-120keV) spectral temperatures as a function of power density.

X-Ray Spectra at Varying Mirror Ratios

Most electron cyclotron resonance ion sources, including LBNL's three sources, rely on the superposition of solenoid and sextupole magnetic fields for plasma confinement. The effect of magnetic field configuration on x-ray spectra has been shown recently [9, 12]. One study carried out in [12] showed that increasing the magnitude of the minimum magnetic field caused the spectral temperature to increase, as well as the maximum energy of the recorded photons. The magnitude of the maximum magnetic field at both injection and extraction were kept approximately constant. Increasing the minimum magnetic field has two effects: a decreased mirror ratio and a smaller magnetic field gradient at the resonance point. Models show (see, for example, [13]) that a lower gradient in the resonance zone should increase the heating efficiency of the electrons. This, in turn, should increase the number of higher energy electrons, and thus the number of recorded photons at larger energies.

The second effect of increasing the minimum magnetic field is a lower mirror ratio which might also lead to an increase in recorded x-ray counts, although not necessarily to an increase in the maximum energy of recorded x-rays. Lowering the mirror ratio increases the size of the loss cone according to

$$\alpha = \arcsin\left[\left(\frac{B_{\min}}{B_{\max}}\right)^{1/2}\right] = \arcsin\left[\left(\frac{1}{R}\right)^{1/2}\right] \quad (9)$$

Where, $R=B_{max}/B_{min}$ is the mirror ratio. In theory, then, a larger number of particles, both electrons and ions, should escape confinement in the mirror field. If the collimation system is designed such that some of the extraction plate is visible to the detector, we would expect an increase in x-ray counts due to the increased number of lost electrons impacting the extraction plate and creating bremsstrahlung. A recorded x-ray spectrum that is made using a collimation system that allows the detector to see the extraction plate will have contributions from both the decreased resonance zone magnetic gradient, and the decreased mirror ratio. Because the detector in [9] could see the extraction plate, the x-ray spectra most likely included both effects. A question that might be asked is: what is the relative importance of these effects?

To answer this we recorded two sets of spectra. Both sets of spectra are taken at the same power level, but at varying extraction mirror ratios. Table 2 summarizes the changes in magnetic field configuration at the extraction plane.

Mirror Ratio (B_{max}/B_{min})	**1.39**	**1.41**	**1.43**	**1.45**
Gradient (Gauss/cm)	69	72	75	78
Bmax (Gauss)	2859	2849	2839	2829
Bmin(Guass)	2056	2021	1986	1950

Table 2. Summary of magnetic field parameters at extraction for the LBNL-ECR ion source.

One set of spectra is taken using the complete collimation system (only plasma visible to the detector), and the other is taken with the last copper collimator, collimator "C" in Figure 2, removed (both plasma and extraction plate visible to detector). The results are shown in Figure 15. With partial collimation there is a definite increase in x-ray counts at higher energies as the mirror ratio is decreased. This increase is most likely due to lost electrons striking the extraction plate and creating bremsstrahlung, though, some portion may be due to the increased heating efficiency at lower magnetic field gradients. With full collimation, however, there is very little change in the spectra as the mirror ratio is changed. Further studies will be undertaken to determine whether the results shown in Figure 15 are real, physical results, or just poor statistics due to the low count rate with full collimation. A more significant change in mirror ratio might also be required to have a larger change in the x-ray spectra in the case of full collimation.

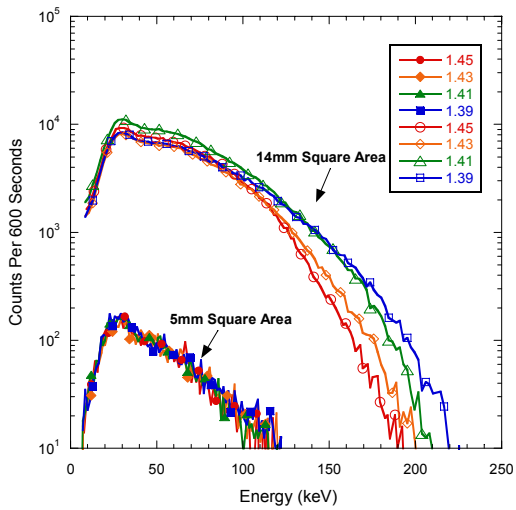

Figure 15. 6.4GHz (LBNL-ECR) spectra at varying mirror ratios. As the mirror ratio increases the amount of counts at the higher energy end increases only when a 14mm square area is visible to the detector at the 8mm diameter circular extraction aperture. This trend is not seen when a 5mm square area is visible.

SUMMARY

The bremsstrahlung spectra presented in this paper are emitted through the extraction end of the LBNL-ECR and VENUS ion sources, which operate at heating frequencies of 6.4GHz, and 18 and 28GHz, respectively. The spectral temperatures and integrated count numbers obtained from the x-ray spectra when varying parameters such as microwave frequency, microwave power, and mirror ratio give insight into the behavior of the electrons in the plasma. Our ultimate goal is to determine the distribution of electron energies in the plasma, and, for this reason, it is important that the recorded bremsstrahlung spectra reflect the spectra emitted by the electrons as accurately as possible. We have shown that a careful collimation geometry of the bremsstrahlung spectra is important. Specifically, the amount of wall bremsstrahlung visible to the detection system can significantly impact the energy and counts of the recorded spectrum.

We have observed trends in the spectra that agree with previous predictions. Increasing power leads to a linear increase in the amount of counts but does not change the spectral temperatures of the spectra. On the other hand, increasing the heating frequency increases the energy of the electrons which is observed in the spectra since they extend to higher energies. Lastly, decreasing the mirror ratio also appears to increase the energy of the observed spectra. We have noted that in this study this last trend was only seen in spectra for which the extraction wall was visible to the detector. An attempt to explain this is made by considering magnetic field gradient at the resonance zone as well as the size of the loss cone. More attention will be paid to this in future studies. In addition to this, future studies will include simultaneous axial and radial bremsstrahlung measurements. Bremsstrahlung measurements from the AECR-U, using 10GHz and 14GHz heating will also be collected.

ACKNOWLEDGEMENTS

The authors would like to thank Dr. David Ward for his invaluable suggestions and help.

This work was supported by the Director, Office of Energy Research, Office of High Energy and Nuclear Physics, Nuclear Physics Division of the U.S. Department of Energy under Contract DE AC03-76SF00098.

REFERENCES

[1] M. Lamoureux, P. Waller, P. Charles, and N.B. Avdonina, Physical Review E **62** (2000) 4091.

[2] M.J. Berger, J.H. Hubbell, S.M. Seltzer, J. Chang, J.S. Coursey, R. Sukumar, D.S. Zucker, " XCOM: Photon Cross Sections Database", [cited 2008 Oct 15], http://physics.nist.gov/PhysRefData/Xcom/Text/XCOM.html

[3] "Efficiency Calculations for Selected Scintillators", Saint-Gobain Crystals, [cited 2008 Oct 15], http://www.detectors.saint-gobain.com/media/documents/S000000000000001004/SGC_Efficiency_Calculations.pdf

[4] P.C. Fisher and L.B. Engle, Physical Review **134** (1964) B796-B816.

[5] D. Ward, H.R. Andrews, B. Haas, P. Taras, and N. Rud, Nuclear Physics **A397** (1983) 161-204.

[6] Nuclear Data Tables, 1960: 59.

[7] "Python Programming Language-Official Website," [cited 2008 Sep 10], http://www.python.org/.

[8] R. Geller, *Electron Cyclotron Resonance Ion Sources and ECR Plasmas*, Bristol: Institute of Physics Publishing, 1998: 252.

[9] D. Leitner, J.Y. Benitez, C.M. Lyneis, D.S. Todd, T. Ropponen, J. Ropponen, H. Koivisto, and S. Gammino, Rev. of Sci. Inst., **79** (2008) 033302.

[10] Z.Q. Xie, Rev. of Sci. Inst., **69** (1998) 625.

[11] A. Girard, C. Pernot, and G. Melin, Physical Review E **62** (2000) 1182.

[12] C.M. Lyneis, D. Leitner, D. Todd, S. Virostek, T. Loew, A. Heinen, O. Tarvainen, Rev. of Sci. Inst., **77** (2006) 03A342.

[13] Y. Jongen, C. Pirate, and G. Ryckewaert, Proceedings of the 6th International Workshop on ECR Ion Sources, Lawrence Berkeley National Laboratory, LBNL, (1985) 238-255.